Soft-phonon feature, site defects, and a frustrated phase transition in $Ni_{50}Ti_{47}Fe_3$: Experiments and first-principles calculations

M. E. Manley,[1,2] M. Asta,[2] J. C. Lashley,[3] C. M. Retford,[2] W. L. Hults,[3] R. D. Taylor,[3] D. J. Thoma,[3] J. L. Smith,[3] R. E. Hackenberg,[3] and K. Littrell[4]

[1]*Lawrence Livermore National Laboratory, Livermore, California 94551, USA*

[2]*Department of Chemical Engineering and Materials Science, University of California, Davis, California 95616, USA*

[3]*Los Alamos National Laboratory, Los Alamos, New Mexico 87545, USA*

[4]*Argonne National Laboratory, Argonne, Illinois 60439, USA*

(Received 19 June 2007; published 3 January 2008)

A soft-phonon feature associated with the shape-memory transition in NiTi is observed in the phonon density of states (DOS) of the *B*2 phase of both NiTi and $Ni_{50}Ti_{47}Fe_3$ (with Fe substituted for Ti) using inelastic neutron scattering. In both alloys, the feature softens with decreasing temperature, but the softening occurs about 100 K lower in the Fe-substituted alloy, indicating a decreased transition temperature. Electrical resistivity and magnetic susceptibility verify the decreased transition temperature but also show that the transition develops second-order-like behavior similar to that observed by others in $Ni_{44}Ti_{50}Fe_6$ (with Fe substituted for Ni). First-principles calculations supported by Mössbauer spectroscopy and neutron diffraction indicate a double-defect scenario, where Fe occupies Ni sites and the displaced Ni occupies the empty Ti sites in the Ti-substituted alloys. A comparison between the current results for Ti-substituted alloys, and related experimental data for alloys featuring Fe substitution for Ni, indicates that the instability temperature is controlled by the number of Fe atoms occupying the Ni sites, while the second-order-like behavior is caused by the addition of the Ni antisite defects. We argue that this latter behavior results from percolated networks of interacting defects acting to frustrate the symmetry-breaking strains.

DOI: 10.1103/PhysRevB.77.024201 PACS number(s): 64.70.K−, 61.72.J−, 76.80.+y, 78.70.Nx

I. INTRODUCTION

The shape-memory effect present in the NiTi intermetallic compound is widely utilized for couplings, fasteners, connectors, and actuators in the automotive and aerospace industries, as well as for electronics and medical applications. This has been, in part, a motivator for considerable theoretical[1–5] and experimental research[6–13] into the mechanisms behind its shape-memory effect. A complete assessment of compositional effects on the physics controlling the relevant phase transitions, however, has not been developed.

Small compositional changes lead to large changes in the thermal stability of the intermediate *R* phase in NiTi-based alloys.[14–16] It has also been reported that the *R* phase does not appear in pure NiTi when samples are annealed,[14–16] suggesting that small amounts of structural disorder may also affect the *R*-phase stability. These effects on the *R*-phase transition might be understood in terms of its underlying mechanism, namely the Fermi-surface nesting.[1,2] One perspective is that disorder, chemical or structural, smears out the Fermi-surface-nested features, analogous to the way temperature does.[1,2] A smearing of the Fermi-surface-nested features might cause a hardening of the associated soft phonon in the *B*2-phase[1,2] and hence drive down the transition temperature. However, electronic effects associated with changes in chemical composition must also play a role, and a complete understanding must account for the interplay between electronic and disorder effects on the soft-phonon instability.

In addition to altering the soft-phonon instability, compositional changes can also change the character of the transition. Recent work by Choi *et al.*[17,18] has shown that the typically first-order *R*-phase transition develops second-order-like behavior in $Ni_{50-x}Ti_{50}Fe_x$ alloys where Fe is substituted for Ni, with $x \geqslant 6$. In particular, Choi *et al.* observe a continuous and reversible transition with no latent heat. Furthermore, they show that this behavior is accompanied by a gradual development of diffuse scattering at an incommensurate position near $1/3\langle 110\rangle$ (followed by a peak locking into the commensurate position for $x=6$) and a suppression of a distortion that usually occurs during the *R*-phase transformation.[18] The result is a higher-symmetry phase they designate the *C* phase and a nanoscale domainlike structure.[18] This effect might be understood by considering another step in the underlying transition sequence:[15,19] cubic (*B*2) → second-order incommensurate charge density wave (CDW) → first-order commensurate CDW (*R* phase) → martensitic phase (*B*19′). Specifically, the strains that bring the incommensurate CDW phase to the commensurate *R* phase may be frustrated by the presence of point defects. The detail of how Fe substitutions, and the associated defects, acts to frustrate these transformation strains remains unclear.

In this article, we examine the precursor soft phonon, the temperature characteristics of the transition, and the local behavior around Fe in a related alloy where Fe is substituted for Ti rather than for Ni. The more complicated compositional disorder inherent in this alloy provides a contrast to the Ni-substituted alloy that allows us to distinguish between disorder and electronic effects on the transition temperature and provides information on the way point defects act to constrain symmetry breaking transformation strains. These observations provide insight on how to tune these transitions and manipulate the strains responsible for the shape-memory effect.

II. METHODS

A. Experimental methods

We prepared rodlike ingots of $Ni_{50}Ti_{50-x}Fe_x$ alloys ($x=0,3$) by the arc-melting and casting technique, annealed them at 950 °C for 50 h, and water quenched them. The rods, ~5 mm dia × 50 mm long, were then sliced lengthwise into 1-mm-thick plates, chemically cleaned, loaded into aluminum "pie pan" sample holders, and measured on the LRMECS time-of-flight chopper spectrometer at IPNS, Argonne National Laboratory. The incident energy was 45 meV and the detector coverage (0°–120°) allowed for momentum transfers spanning several Brillouin zones. Spectra were obtained on both alloys at 300 K, 375 K, 475 K, and 575 K. The data were corrected by subtracting the scattering from an empty can and a time-independent background from the data and then summing over the scattering angles.

Temperature characteristics of the phase transition in $Ni_{50}Ti_{47}Fe_{03}$ were examined using electrical-resistivity and magnetic-susceptibility measurements made in a Quantum Design magnetic properties measurement system. Resistivity measurements were performed with and without an applied magnetic field using a standard four-probe technique. Magnetic susceptibility measurements were performed using a vibrating sample magnetometer with an external field of 5 T.

The Mössbauer-effect (ME) in ^{57}Fe was used to study the local behavior of Fe in the $Ni_{50}Ti_{47}Fe_{03}$ alloy at several temperatures. A 1-mm-thick disk of the alloy was polished down to about 30 μm, a thickness that would pass some of the 14.4-keV ME γ rays yet be thick enough to provide a measurable effect. A $^{57}Co(Rh)$ unsplit source at the sample temperature provided the analyzing ME γ rays.

B. First-principles calculation methods

First-principles calculations were undertaken to compute the structural and energetic properties associated with the substitution of Fe for Ni and Ti in the $B2$ phase of NiTi. Calculations were undertaken using the projector augmented-wave (PAW) method[20,21] and the Perdew-Becke-Ernzerhof generalized gradient approximation[22] (PBE-GGA) as implemented in the VASP (Vienna *ab initio* simulation package) code.[23,24] Use was made of the PAW potentials labeled "Fe," "Ti," and "Ni" in the VASP PBE library, and for Fe and Ti this choice leads to treatment of the semicore $3p$ states as core electrons. The electronic wave functions were expanded in plane waves with a cutoff of 337 eV. Structural optimizations were undertaken until the forces on the atoms converged to within 0.01 eV/Å. Relaxed atomic structures were derived from calculations employing an "equivalent" k-point sampling technique[25] and the Methfessel-Paxton broadening scheme[26] with k-point meshes equivalent to a $12\times12\times12$ grid for the primitive $B2$ structure and a smearing of 0.1 eV. The final total energies presented below for relaxed and unrelaxed geometries were obtained from a final calculation employing tetrahedron integration with a k-point density equivalent to a $24\times24\times24$ mesh for the primitive $B2$ crystal structure. Convergence checks were performed employing larger k-point densities and smaller smearing parameters, leading to an estimated convergence of the relaxed bond lengths to within a few hundredths of an Å and differences in defect energies (see below) converged to within 0.01 eV. All calculations were performed spin polarized. For the largest defect Fe-containing supercells (1 Fe per 216 atoms) negligible magnetic moments were obtained for both relaxed and unrelaxed structures. Finite moments as large as $2\mu_B$ per Fe atom were calculated in some of the smaller supercells (with higher Fe concentrations), although the exact nature of the magnetic structure was found to depend sensitively on the defect concentration and atomic configuration.

III. RESULTS AND ANALYSIS

A. Experimental results

The neutron-scattering spectra were corrected for incoherent multiphonon scattering determined iteratively to all orders, the elastic peak, and the thermal occupation factor using a procedure described in detail elsewhere.[27] The resulting cross-section weighted phonon densities of states (DOS) are shown in Fig. 1. A dominant feature between 15 and 20 meV appears broader and stiffer in the Fe-substituted alloy at temperatures of 375 K and higher. This is likely caused by the addition of slightly stiffer Fe modes relative to Ni modes in the Fe-substituted alloy (see the calculated partial phonon DOS of Ni and Fe in a similar alloy.[28]) A particularly temperature-dependent feature appears near 8.5 meV in NiTi at 575 K and in approximately the same position in $Ni_{50}Ti_{47}Fe_3$ at 475 K, as indicated by the black (NiTi) and gray ($Ni_{50}Ti_{47}Fe_3$) arrows in Fig. 1. In both alloys, the feature softens with decreasing temperature, with the $Ni_{50}Ti_{47}Fe_3$ continuing to show the feature at the same position ~100 K lower in temperature. Neutron-diffraction patterns indicate that between 375 K and 300 K the NiTi alloy goes through its well-known martensitic transition ($B19'$), and the changes observed in the phonon DOS are also similar to those observed previously for this transition by Bogdanoff and Fultz.[12] The neutron-diffraction patterns for $Ni_{50}Ti_{47}Fe_3$ show no transformation in this temperature range. This is not surprising if we identify the softening phonon feature below 10 meV with the precursor phonon mode to the R-phase transition.[6,7] The softening of this mode also triggers the transition sequence (through the intermediate R phase) that eventually leads to the martensitic phase,[19] and since it appears in the same position about 100 K lower in $Ni_{50}Ti_{47}Fe_3$ than in NiTi, we expect the transition to also be lowered by about 100 K.

Electrical-resistivity and magnetic-susceptibility measurements were used to search for a lower-temperature transition indicated by the phonons in the $Ni_{50}Ti_{47}Fe_3$ alloy. As shown in the top panel of Fig. 2, a minimum occurs in the electrical resistivity around 260 K, about the temperature where the phonons would suggest a transition. On further cooling, the resistivity increases to a broad maximum, and this effect is independent of an applied magnetic field and reversible on heating and cooling. The magnetic-field independence eliminates the possibility of scattering from magnetic impurity sites (Kondo). Since the phonon scattering is decreasing with

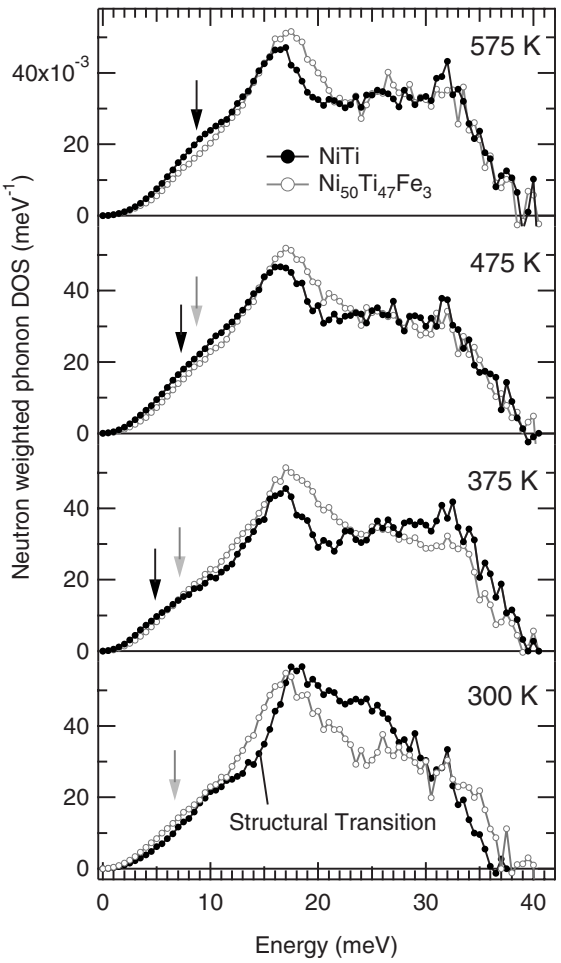

FIG. 1. Temperature dependence of the phonon density of states (DOS) extracted from spectra collected using the LRMECS time-of-flight spectrometer at the Intense Pulsed Neutron Source (see text for details). Arrows indicate the position of a particularly temperature-dependent feature in both alloys.

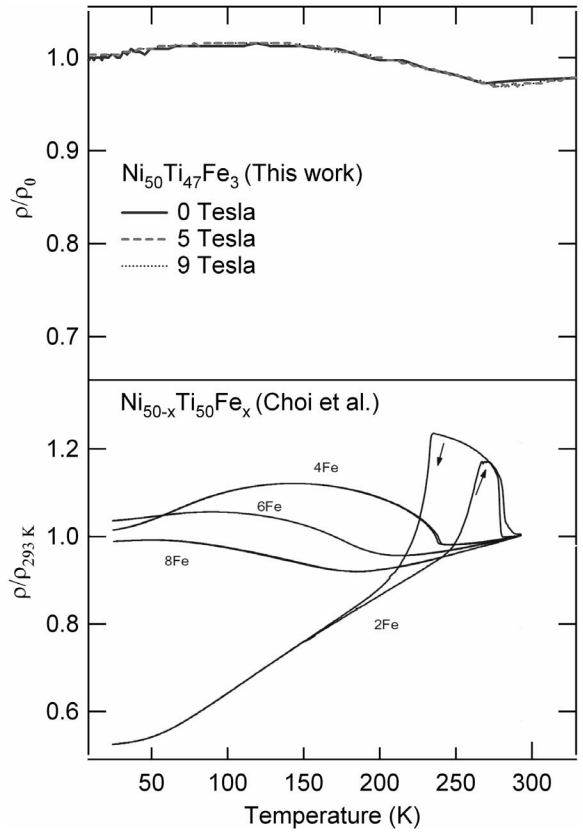

FIG. 2. Temperature and magnetic-field dependence of the electrical resistivity measured on our $Ni_{50}Ti_{47}Fe_3$ sample (top) along with the results of Choi *et al.* (Ref. 18, bottom) on a series of $Ni_{50-x}Ti_{50}Fe_x$ samples (no magnetic field).

temperature as the phonons become depopulated, this implies a gradual development of structural changes on cooling. This smooth and continuous behavior is very similar to the second-order-like behavior described by Choi *et al.*[17,18] in $Ni_{50-x}Ti_{50}Fe_x$ alloys involving Fe substitution for Ni, with x near 6. For comparison their results are reproduced in the bottom panel of Fig. 2. Notable differences with our Ti-substituted alloy are that the second-order-like behavior is occurring at half the Fe concentration and at a higher temperature. In fact, the onset temperature of the behavior, 260 K, is about where the transition is expected in the Ni-substituted alloys $Ni_{50-x}Ti_{50}Fe_x$, with the same amount of Fe, $x=3$ (note that 260 K is between the transition temperatures for $x=2$ and 4 in the data of Choi *et al.* in Fig. 2), so the main difference between Ni and Ti substitution appears to be the onset of the second-order-like behavior at a lower Fe concentration. Our resistivity minimum also appears slightly sharper.

The magnetic susceptibility versus temperature curve of $Ni_{50}Ti_{47}Fe_3$, shown in the top panel of Fig. 3, is also qualitatively similar to $Ni_{50-x}Ti_{50}Fe_x$ alloys (bottom panel) with x near 6, but again the main feature appears at a higher temperature, which in this case is a shoulder about 50 K below the resistivity minimum. The lack of any Curie tail (a $1/T$ term that is obvious at low temperatures) in the magnetic susceptibility also indicates that there are no significant local moments and thus that the Fe is in solution.

Mössbauer-effect spectra taken at 4 K and 300 K, and at a high and low Doppler velocity, are shown in Fig. 4. The data were least-squares fitted with a program that allows both magnetic and quadrupole interactions constrained to the hyperfine transitions allowed in the ^{57}Fe ME. The line shape of the central peak, examined at the Doppler velocity scans of ±3 mm/s, showed quadrupole broadening of the basic Lorentzian amounting to 0.44 (6) mm/s. The field gradient at the Fe can arise from a noncubic local structure in the alloy or from the local variations of the Ni-Ti neighbors about the ME probe. No magnetic hyperfine splitting was observed, indicating that no magnetic species is present, consistent with the magnetic-susceptibility measurements. At room temperature, the observed spectra, including the isomer shift (−0.3 mm/s), were similar to those previously observed for $Ni_{47}Ti_{50}Fe_3$, where Fe resides on Ni sites.[29] Since the isomer shift is sensitive to the local chemical environment,[30] this raises the possibility that Fe in $Ni_{50}Ti_{47}Fe_3$ might occupy the Ni sites despite the fact that it was substituted for Ti (this is considered in detail below).

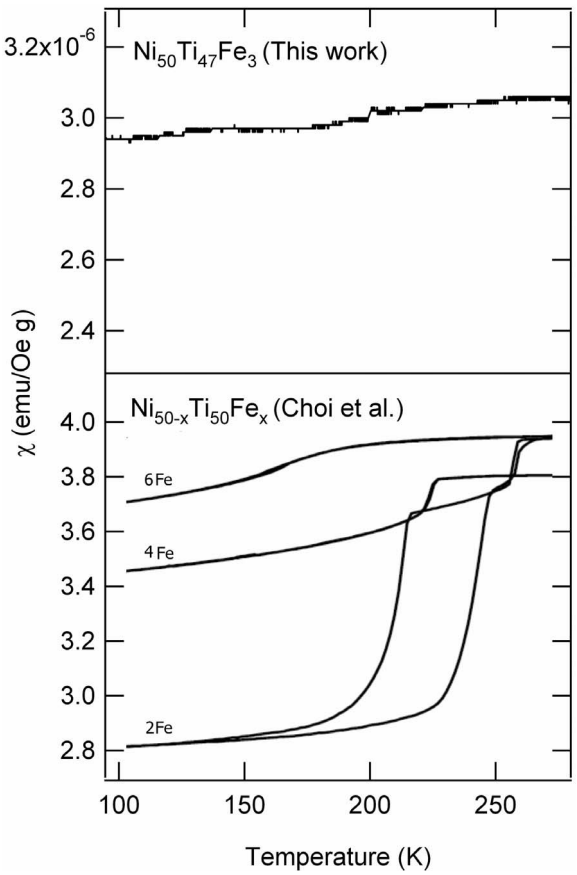

FIG. 3. Temperature dependence of the magnetic susceptibility measured on our $Ni_{50}Ti_{47}Fe_3$ sample along with the results of Choi *et al.* (Ref. 17) on $Ni_{50-x}Ti_{50}Fe_x$ samples (bottom).

While the Ni-substituted alloy ($Ni_{47}Ti_{50}Fe_3$) exhibits a clear splitting of the central ME peak,[29] the Ti-substituted alloy ($Ni_{50}Ti_{47}Fe_3$) does not, Fig. 4. The splitting of this peak has been attributed to the rhombohedral symmetry of the premartensitic *R* phase.[29] The lack of any splitting lends further support to the suggestion that the transition in $Ni_{50}Ti_{47}Fe_3$ is behaving similarly to the transition in $Ni_{50-x}Ti_{50}Fe_x$ alloys with x near 6. As shown by Choi *et al.*,[18] the second-order-like behavior in $Ni_{50-x}Ti_{50}Fe_x$ alloys with $x \geqslant 6$ is accompanied by the restraint of a distortion of the lattice that accompanies the *R*-phase transition.

B. First-principles calculation results

To understand the origins of the observed compositional effects on structural transitions it is desirable to confirm the site selection preferences for the Fe solute atoms and determine the nature of the local structural distortions that they induce. To this end, first-principles calculations were undertaken employing the methods described in Sec. II B. For the $Ni_{50}Ti_{50-x}Fe_x$ *B*2 alloys investigated in this work, two scenarios were considered for the defects resulting from Fe additions: (i) a single-defect scenario—the addition of an Fe atom leads to the formation of single Fe impurity replacing Ti on its sublattice with an associated defect energy $\Delta E_{\mathrm{Fe}}^{\mathrm{Ti}}$—and (ii) a double-defect scenario—Fe replaces Ni on its sublattice and the excess Ni required to maintain the composition replaces Ti with a total associated defect energy of $(\Delta E_{\mathrm{Fe}}^{\mathrm{Ni}}+\Delta E_{\mathrm{Ni}}^{\mathrm{Ti}})$, where $\Delta E_{\mathrm{Ni}}^{\mathrm{Ti}}$ is the energy to form a Ni antisite defect on the Ti sublattice and $\Delta E_{\mathrm{Fe}}^{\mathrm{Ni}}$ is the energy to replace Ni with Fe.

To determine the relative stability of the different defect structures (i) and (ii) we performed calculations of each of the impurity energies (ΔE_I^J) defined above, employing periodic supercell structures at fixed volume. Specifically, to compute a value for ΔE_I^J we consider an *N*-atom periodic supercell of pure NiTi and replace a single atom of type *J* by the defect atom *I*. The formation energy is then derived from the difference in energy (per point defect) between this defect supercell and a pure NiTi structure with the same total number of atoms. Note that with this definition, ΔE_I^J is derived from the difference in energy between two structures containing different relative numbers of each atomic species (Ni, Ti, or Fe) and thus contains contributions associated with the chemical potentials of the different atom types. However, this dependence on chemical potential drops out in the difference $\Delta E_{\mathrm{Fe}}^{\mathrm{Ti}}-(\Delta E_{\mathrm{Fe}}^{\mathrm{Ni}}+\Delta E_{\mathrm{Ni}}^{\mathrm{Ti}})$, which determines the relative stability of the single versus double-defect structures.

Table I lists calculated values of $\Delta E_{\mathrm{Fe}}^{\mathrm{Ti}}-(\Delta E_{\mathrm{Fe}}^{\mathrm{Ni}}+\Delta E_{\mathrm{Ni}}^{\mathrm{Ti}})$ obtained from supercells containing $N=54$, 128, and 216 atoms. Positive (negative) values indicate a preference for the double (single) defect. As N is increased the separation between the impurities and their nearest periodic images also increases; for $N=54$, 128, and 216, the point defects are spaced at distances $r=3a=9.012$ Å, $r=4a=12.016$ Å, and $r=3\sqrt{3}a=15.609$ Å, where $a=3.004$ Å is the calculated zero-temperature lattice constant for NiTi. The trend in the energies as a function of N provides an indication of the range of interactions between the defects. The calculated results in Table I are given for both unrelaxed structures, where the atoms are forced to maintain their ideal positions corresponding to a perfect stoichiometric NiTi *B*2 cubic structure, and for fully relaxed structures, where the positions of the atoms relax off of these ideal positions to achieve a local minimum in the energy under the constraint of a fixed supercell volume. The results of the unrelaxed calculations give an indication of the "chemical" effects driving site-selection behavior, while the results of the relaxed calculations include additional contributions arising from relaxation of the solute-induced strain energy and associated defect interactions mediated by the displacement fields.

Considering first the results of unrelaxed calculations, we note that $\Delta E_{\mathrm{Fe}}^{\mathrm{Ti}}-(\Delta E_{\mathrm{Fe}}^{\mathrm{Ni}}+\Delta E_{\mathrm{Ni}}^{\mathrm{Ti}})$ is positive and on the order of 1.0 eV, indicating a strong chemical preference for the double-defect structure. The results from the relaxed calculations confirm this preference, although they display a somewhat slower convergence with respect to system size. Specifically, the energy difference $\Delta E_{\mathrm{Fe}}^{\mathrm{Ti}}-(\Delta E_{\mathrm{Fe}}^{\mathrm{Ni}}+\Delta E_{\mathrm{Ni}}^{\mathrm{Ti}})$ decreases by 0.24 eV as the distance between the defects increases from 9.012 to 15.609 Å in the relaxed calculations. The convergence is found to be even slower for the energies of the individual defects on the Ti sublattice, with $\Delta E_{\mathrm{Ni}}^{\mathrm{Ti}}$ and $\Delta E_{\mathrm{Fe}}^{\mathrm{Ti}}$ decreasing by roughly 2.5 eV over this same range of distance. By contrast, the relaxed value of $\Delta E_{\mathrm{Fe}}^{\mathrm{Ni}}$ converges

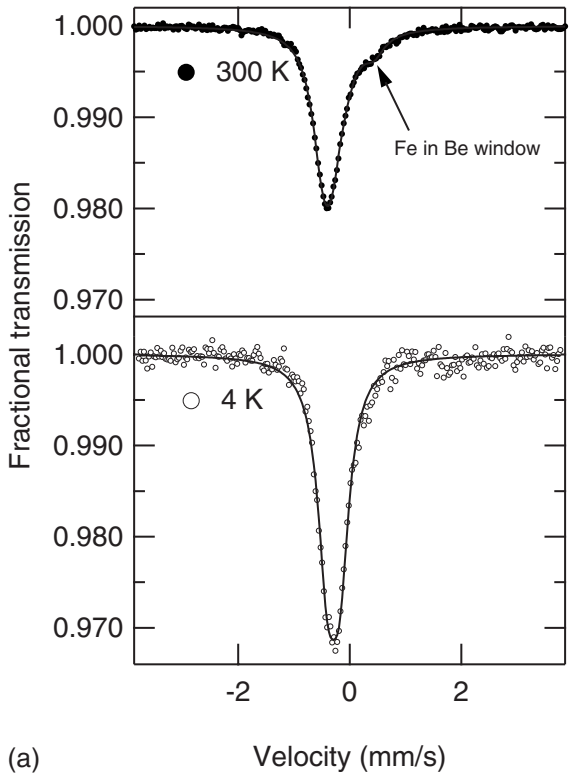

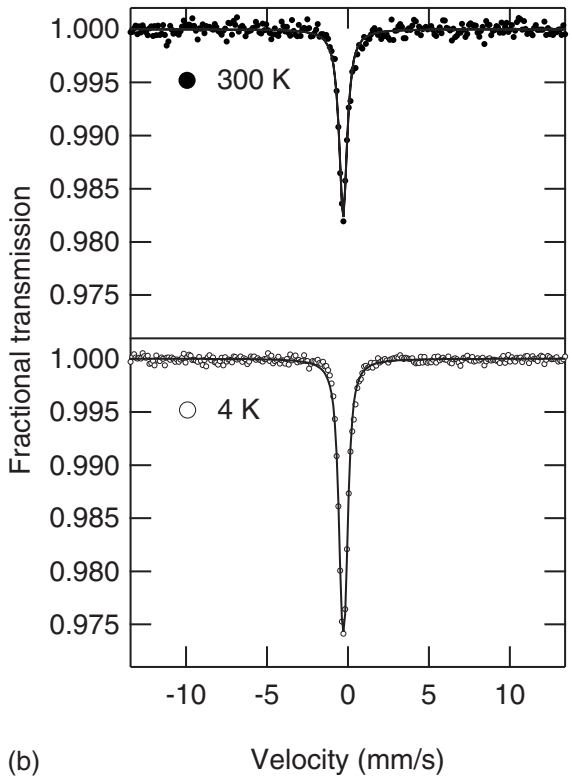

FIG. 4. Mössbauer-effect absorption spectra observed at 4 K and 300 K for (a) a low Doppler velocity and (b) a high Doppler velocity. The small feature indicated in the low-speed 300 K spectra (Fe in Be window) is from Fe impurities in the Be windows of the cryostat. The solid lines are fit to the data using a procedure described in the text.

TABLE I. Energy cost of forming single Fe defects on the Ti sublattice versus a double-defect scenario with Fe on the Ni sublattice and the excess Ni on the Ti sublattice for different supercell sizes (see text).

		$\Delta E_{\mathrm{Fe}}^{\mathrm{Ti}}-(\Delta E_{\mathrm{Fe}}^{\mathrm{Ni}}+\Delta E_{\mathrm{Ni}}^{\mathrm{Ti}})$ eV	
N	R (Å)	Unrelaxed	Relaxed
54	9.01	0.95	0.71
128	12.02	1.00	0.42
216	15.61	0.96	0.47

relatively rapidly with supercell size, varying by less than 0.1 eV over the range of N (54–216 atoms) considered in these calculations.

The slow convergence of the Ti sublattice defect energies is associated with the formation of large elastic displacement fields around these defects. Figure 5 plots the calculated displacements surrounding the different point defects considered in this work, which are derived from a 216-atom supercell. In this plot the vertical axis indicates the change in bond length, plotted versus neighbor shell on the horizontal axis. For an Fe impurity on the Ni sublattice, the strain field decays rapidly, becoming negligible beyond the first-neighbor shell. By contrast, replacing Ti by either Fe or Ni results in large oscillating displacements that do not decay appreciably out to the maximum distance probed in the supercell (half the distance between the periodic images of the defects). Around an Fe or Ni impurity on the Ti sublattice, the structural distortions involve an elongation of the bonds with the nearest-neighbor Ni atoms and a contraction of the bonds with the second-neighbor Ti atoms. These distortions are sufficiently large to give rise to an equilibrium second-neighbor impurity-Ti bond length that becomes shorter than the nearest-neighbor impurity-Ni bond length. These results are indicative of a strong repulsion between Ni-Ni and Ni-Fe nearest neighbors and a strong attraction of Ti with Fe and Ni in these defect configurations.

For completeness, we note that in addition to the two defect scenarios considered above, other possible defect configurations can be envisioned involving constitutional vacancies. We considered one such defect complex involving two Ti vacancies and an Fe substitution for a Ni that gives rise to much higher formation energies than either of the defect structures considered above. Overall, the first-principles calculations suggest that the atomic configurations in $Ni_{50}Ti_{50-x}Fe_x$ are characterized by the presence of a total point-defect concentration of twice x, with Ni antisites on the Ti sublattice and Fe impurities on the Ni sublattice, Fig. 5. This result is consistent with the experimental observations. First, the ME spectra indicate that the chemical environment of the Fe is similar to that of $Ni_{47}Ti_{50}Fe_3$ where it is expected to reside on the Ni sublattice. Second, the neutron-diffraction data showed only a slight contraction of lattice parameter ($\sim$0.3%) with the Fe substitution, ruling out the existence of large concentrations of vacancies.

IV. DISCUSSION

Despite the predicted double number of site defects, the soft-phonon instability temperature (transition to R or C

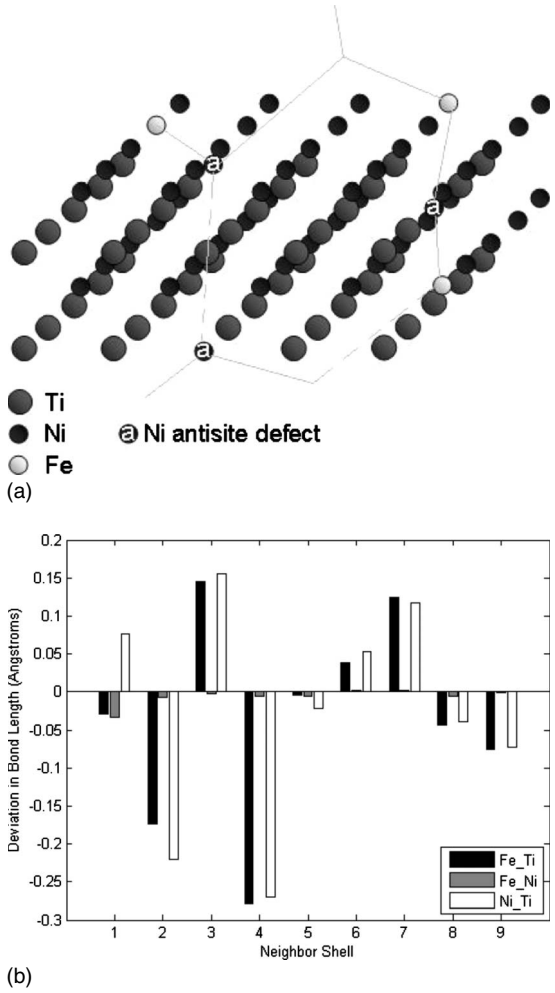

FIG. 5. Double-defect scenario (a) deduced using a first-principles calculation based on the GGA and supported by Mössbauer-effect spectroscopy and neutron-diffraction results. Shown in (b) are the respective displacements of the first nine nearest neighbors around three site defect types, Fe on a Ti site (Fe-Ti), Fe on a Ni site (Fe-Ni), and Ni on Ti site (Ni-Ti). Gray lines connecting site defects in (a) show how interactions might form a percolated network.

phase) in the Ti-substituted alloy $Ni_{50}Ti_{47}Fe_3$ is essentially the same as in the Ni-substituted alloy $Ni_{47}Ti_{50}Fe_3$. This implies that the phonon instability temperature is determined primarily by the number of Fe atoms on the Ni sites and is relatively insensitive to the extra Ni antisite defects. Furthermore, this implies that the disorder-induced blurring of the nesting feature in the Fermi surface[1,2] from the addition of Ni antisite defects is less important than the chemical effect of swapping out Ni atoms for Fe atoms in determining the phonon instability temperature.

By contrast, the characteristics of the transition are strongly influenced by the presence of the Ni antisite defects. The characteristic shape of the resistivity versus temperature and the magnetic-susceptibility versus temperature curves and the suppression of a structural distortion observed for $Ni_{50}Ti_{47}Fe_3$ are qualitatively similar to those observed for Choi *et al.* for $Ni_{44}Ti_{50}Fe_6$ and not $Ni_{47}Ti_{50}Fe_3$. It is interesting that similar behavior observed with Ni substitutions for Ti in $Ni_{50+x}Ti_{50-x}$ alloys with $x>1$ has been shown to have the characteristics of a strain glass,[31] where the transition strains are frustrated by point defects and the superlattice diffraction peaks are frozen into incommensurate positions below a glass transition temperature defined in Ref. 31. However, $Ni_{50}Ti_{47}Fe_3$ and $Ni_{44}Ti_{50}Fe_6$ exhibit similar behavior at different temperatures but with a common number of site defects.

A critical site-defect concentration for strain frustration suggests a percolation limit, perhaps for defect-defect interactions. Consider a network of interacting site defects that percolate throughout crystalline regions above a critical concentration, which are the gray lines in Fig. 5. These networks could cause local orientation preferences for distorting into one of the eight equivalent strain variants for $B2$ $(Pm3m)$ to R $(P3)$, thereby frustrating the transformation strains.[31] This mechanism might also explain the nanoscale domainlike structure observed in $Ni_{44}Ti_{50}Fe_6$ below the transition temperature.[18] It is interesting that similar nanoscale domains also appear in the $Ni_{52}Ti_{48}$ strain-glass state.[31] However, for this same mechanism to be operating in this alloy longer-range defect-defect interactions are needed to compensate for the lower concentration. Indeed, according to the relaxation results in Fig. 5, the range of Ni antisite defects is considerably longer than for Fe on Ni sites, so the defect-defect interactions are expected to bridge larger distances and thus form networks at a lower concentration. Effects of site-defect clustering and/or short-range order might also play a role. Nevertheless, it is likely that $Ni_{50+x}Ti_{50-x}$ $(x=2)$, $Ni_{50}Ti_{50-x}Fe_x$ $(x=3)$, and $Ni_{50-x}Ti_{50}Fe_x$ $(x=6)$ are all exhibiting the same frustrated transition strain or "strain-glass" state, but with slightly different defect constraint conditions.

V. CONCLUSIONS

Our results show that compositional effects can act to change aspects of the shape memory and related transitions in NiTi in complex ways that depend on both defect chemistry and structure. Substitutions of Fe on the Ni sublattice drive down the temperature of the soft-phonon instability independent of whether or not Ni antisite defects are present. On the other hand, the Ni antisite defects contribute to frustrating the symmetry-breaking transition strains. Comparison with other work suggests that this strain-glass state[30] forms with at least three different defect site configurations. All of these can be qualitatively understood in terms of percolated networks of interacting defects, provided that adjustments are made for the different defect-defect interaction ranges.

ACKNOWLEDGMENTS

M.E.M. would like to thank S. McCall for useful discussions and M. Kresch for technical assistance with the neutron-scattering data reduction. M.A. and C.M.R. would like to thank B. Haley and N. Gronbech-Jensen for useful discussions and assistance with preliminary VASP calculations. This work was supported by the U.S. Department of

Energy under Contracts Nos. W-31-109-ENG-38, W-7405-ENG-36, and DE-AC52-06NA25396. Work was performed under the auspices of the U.S. Department of Energy by the University of California, Lawrence Livermore National Laboratory under Contract No. W-7405-Eng-46. This work was also performed under the auspices of the Materials Design Institute, a Los Alamos-UC Davis Educational Collaboration, LANL Subcontract No. 25110-002-06.

[1] G. L. Zhao, T. C. Leung, B. N. Harmon, M. Keil, M. Mullner, and W. Weber, Phys. Rev. B **40**, 7999 (1989).
[2] G. L. Zhao and B. N. Harmon, Phys. Rev. B **48**, 2031 (1993).
[3] X. Huang, C. Bungaro, V. Godlevsky, and K. M. Rabe, Phys. Rev. B **65**, 014108 (2001).
[4] K. Parlinski and M. Parlinska-Wojtan, Phys. Rev. B **66**, 064307 (2002).
[5] X. Huang, C. Bungaro, G. J. Ackland, and K. M. Rabe, Nat. Mater. **2**, 307 (2003).
[6] P. Moine, J. Allain, and B. Renker, J. Phys. F: Met. Phys. **14**, 2517 (1984).
[7] H. Tietze, M. Mullner, and B. Renker, J. Phys. C **17**, L529 (1984).
[8] S. K. Satija, S. M. Shapiro, M. B. Salamon, and C. M. Wayman, Phys. Rev. B **29**, 6031 (1984).
[9] M. B. Salamon, M. E. Meichle, and C. M. Wayman, Phys. Rev. B **31**, 7306 (1985).
[10] H. Tietze, M. Mullner, P. Selgert, and W. Assmus, J. Phys. F: Met. Phys. **15**, 263 (1985).
[11] Y. Murakami and D. Shindo, Mater. Trans., JIM **40**, 1092 (1999).
[12] P. D. Bogdanoff and B. Fultz, Philos. Mag. B **81**, 299 (2001).
[13] D. Shindo, Y. Murakami, and T. Ohba, MRS Bull. **27**, 121 (2002).
[14] H. C. Ling and R. Kaplow, Metall. Trans. A **11**, 77 (1980); Metall. Trans. A **12**, 2101 (1981).
[15] C. M. Huang, M. Meichle, M. B. Salamon, and C. M. Wayman, J. Phys. (Paris), Colloq. **43**, C4–231 (1982); Philos. Mag. A **47**, 31 (1983).
[16] E. Goo and R. Sinclair, Acta Metall. **33**, 1717 (1985).
[17] M.-S. Choi, T. Fukuda, and T. Kakeshita, Scr. Mater. **53**, 869 (2005).
[18] M.-S. Choi, T. Fukuda, T. Kakeshita, and H. Mori, Philos. Mag. **86**, 67 (2006).
[19] C. M. Wayman (unpublished).
[20] P. E. Blöchl, Phys. Rev. B **50**, 17953 (1994).
[21] G. Kresse and D. Joubert, Phys. Rev. B **59**, 1758 (1999).
[22] J. P. Perdew, K. Burke, and M. Ernzerhof, Phys. Rev. Lett. **77**, 3865 (1996).
[23] G. Kresse and J. Hafner, Phys. Rev. B **47**, R558 (1993).
[24] G. Kresse and J. Hafner, J. Phys.: Condens. Matter **6**, 8245 (1994).
[25] S. Froyen, Phys. Rev. B **39**, 3168 (1989).
[26] M. Methfessel and A. T. Paxton, Phys. Rev. B **40**, 3616 (1989).
[27] M. E. Manley, R. J. McQueeney, B. Fultz, R. Osborn, G. H. Kwei, and P. D. Bogdanoff, Phys. Rev. B **65**, 144111 (2002).
[28] D. Góra and K. Parlinski, J. Phys. Chem. Solids **66**, 1748 (2005).
[29] M. Jimenez, S. Aburto, R. Gomez, V. Marquina, J. L. Marquina, and D. Rios-Jara, Hyperfine Interact. **66**, 345 (1991).
[30] R. Ingalls, H. G. Drickamer, and G. De Pasquali, Phys. Rev. **155**, 165 (1967).
[31] S. Sarkar, X. Ren, and K. Otsuka, Phys. Rev. Lett. **95**, 205702 (2005).